



Sn@SnO_x/C nanocomposites prepared by oxygen plasma-assisted milling as cyclic durable anodes for lithium ion batteries



Hui Liu, Renzong Hu, Wei Sun, Meiqin Zeng, Jiangwen Liu, Lichun Yang, Min Zhu*

School of Materials Science and Engineering, South China University of Technology, Key Laboratory of Advanced Energy Storage Materials of Guangdong Province, Guangzhou 510640, PR China

HIGHLIGHTS

- Sn@SnO_x/C anodes by oxygen plasma-assisted milling (O₂-P-milling).
- One-step, environmentally friendly and high-efficiency synthesis.
- Sn nanoparticles coated by amorphous-nanocrystalline SnO_x embedded in graphite.
- Superior electrochemical performance with high capacity and stable cyclability.

ARTICLE INFO

Article history:

Received 19 March 2013

Received in revised form

28 April 2013

Accepted 20 May 2013

Available online 28 May 2013

Keywords:

Anode
Lithium ion batteries
Milling
Oxygen plasma
Tin oxides

ABSTRACT

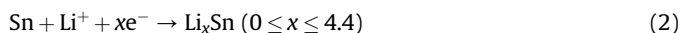
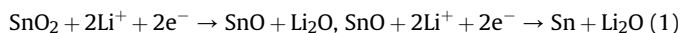
An advanced tin oxide-coated tin in graphite (Sn@SnO_x/C) nanocomposite is synthesized with a one-step method of dielectric barrier discharge oxygen plasma-assisted milling (O₂-P-milling). Synergetic effects of rapid plasma heating and impact stress act on the tin/graphite powder during O₂-P-milling, and SnO_x ($1 \leq x \leq 2$) is generated *in situ* on the Sn surface from the reaction between Sn and oxygen. The resulting composite possesses a unique microstructure, where Sn nanoparticles coated by an ultrathin amorphous/nanocrystalline SnO_x layer are homogeneously embedded within a graphite matrix. As lithium ion anodes, the Sn@SnO_x/C nanocomposites display superior electrochemical performance to Sn–C and Sn–SnO₂–C nanocomposites milled under argon plasma. The SnO_x/C nanocomposite obtained after O₂-P-milling for 25 h that contains a high content of amorphous/nanocrystalline SnO_x exhibits a high capacity retention of 500 mA h g^{−1} at 250 mA g^{−1} after 70 cycles, indicating that O₂-P-milling is a promising method to prepare Sn-based multiphase nanocomposite anode materials.

© 2013 Elsevier B.V. All rights reserved.

1. Introduction

Lithium ion batteries are important power sources in portable electronics and electric vehicles. Graphite materials are widely used as anodes in commercial lithium ion batteries because of their stable cycling performance and low cost. However, the limited capacity of graphite (372 mA h g^{−1}) cannot meet the ever-growing requirements for high-performance lithium ion batteries. Accordingly, Sn-based materials, are promising anode candidates to replace graphite because Sn can react with Li to form Li₂₂Sn₅ alloy, showing a high theoretical capacity (Sn, 992 mA h g^{−1}) [1]. However, the large volume changes generated during Sn alloying/dealloying with Li can lead to pulverization of the electrode and rapid capacity decay, which is a major disadvantage of Sn-based

anodes. Tin oxides can also be used as lithium storage materials. The reaction mechanism involves the following processes [2,3]:



The theoretical capacities of SnO and SnO₂ can be as high as 875 mA h g^{−1} and 782 mA h g^{−1}, respectively. Although their capacities are lower than that of Sn, the Li₂O formed in reaction (1) can serve as a matrix to accommodate the volume change of the active Sn phase and prevents Sn from aggregating. Therefore, it is obvious to consider the strategy of combining Sn with SnO_x ($1 \leq x \leq 2$) in an anode to maintain the reversible capacity and improve the cyclability [4–6].

Extensive research has indicated that dispersing an amorphous/nanostructured Sn-based material in a carbon matrix is an effective way to accommodate the large volume change of Sn [7–10].

* Corresponding author. Tel.: +86 20 87113924; fax: +86 20 87111317.
E-mail address: memzhu@scut.edu.cn (M. Zhu).

Amorphous or nanostructured Sn-based materials tolerate significant expansion instead of cracking and pulverizing like crystalline materials, while carbon matrix prevents aggregation of the Sn-based material and maintains conductive network for the active phases. Therefore, Sn-based carbon composites show enhanced electrochemical performance [11–13]. It has been reported that amorphous/nanostructure Sn–M–C (M = Co, Mn, Fe) alloys were prepared by mechanical attriting, and amorphous Sn–Co–C exhibited good electrochemical property with a capacity of about 400 mA h g^{-1} after 100 cycles [14–16]. Composites of hollow or porous Sn/C, SnO/C, SnO₂/C and Sn/SnO_x/C have been extensively fabricated by chemical deposition assisted with template synthesis [17–23], hydrothermal method [24,25], electrospinning [26–28] and so forth to improve the cyclic stability. However, these composites possess low tap density because of the insufficient filling, which would reduce the energy density for the application of lithium ion battery. Furthermore, these synthesis processes often include complicated steps (such as template removing, temperature controlling, solution concentration adjusting), and offer limited throughput.

Mechanical alloying (MA) is a simple, effective and eco-friendly method for mass production. In our previous study, we prepared Sn–C nanocomposites on a large scale by dielectric barrier discharge argon plasma-assisted milling (P-milling) [29]. Multi-scale Sn particles embedded in the highly crystalline graphite and the composite exhibited a high capacity of 400 mA h g^{-1} for 40 cycles. In this work, we developed a new MA method based on P-milling, namely oxygen plasma-assisted milling (O₂-P-milling). The synthetic procedure is schematically illustrated in Fig. 1. During O₂-P-milling, significant synergy between the effects of rapid heating by the plasma and milling impact stress is exerted on the Sn/graphite powders, and amorphous/nanostructured SnO_x ($1 \leq x \leq 2$) are formed *in situ* due to the reaction of Sn with oxygen. Besides, *in situ* formed SnO_x particles can serve as a grinding aid to refine and disperse Sn particles. Hence, an Sn@SnO_x/C composite with an amorphous/nanostructured Sn core coated by a thin, rigid SnO_x shell embedded in a carbon matrix would be synthesized in one-step by O₂-P-milling. During charge–discharge cycles, SnO_x shell would transform into Li₂O (Eq. (1)) *in situ* on the surface of Sn core, which can restrict swelling of Sn effectively. Therefore, the continual breakdown and reformation of the solid–electrolyte–interface (SEI) is suppressed, and the electric contact between the electrode and matrix is maintained [30,31], which would enable the Sn@SnO_x/C composite to exhibit high capacity and good cyclability.

2. Experimental

2.1. Preparation of Sn@SnO_x/C composites

Details of P-milling are reported in our previous papers [29,32,33]. In this work, oxygen plasma, instead of argon plasma, was generated in the milling cylinder during O₂-P-milling. The raw materials were graphite with a particle size of 400 mesh and Sn powder with a particle size of 100 mesh. Powder mixtures with an Sn:C ratio of 1:1 (w:w) were treated by O₂-P-milling for 2, 5, or 10 h, yielding samples denoted as Sn@SnO_x/C-2 h, Sn@SnO_x/C-5 h, and Sn@SnO_x/C-10 h, respectively. The weight ratio of ball to powder was 50:1. Additional oxygen (0.08 mol) was supplied to the system every 2.5 h to compensate for the continuous consumption of oxygen during the milling process. To further study the influence of SnO_x, the powder mixture was treated by O₂-P-milling for 25 h with an addition of oxygen (0.08 mol) every 5 h, to form the SnO_x/C composite. For comparison, an Sn–50 wt%C composite studied previously [29] and a powder mixture with an SnO₂ (particle size:

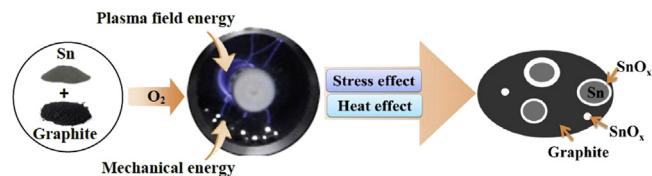


Fig. 1. Synthetic procedure used to prepare Sn@SnO_x/C composites.

50 nm):Sn:C ratio of 5:45:50 (w:w:w) were treated by P-milling for 10 h; these samples are denoted Sn–C and Sn–SnO₂–C, respectively.

2.2. Microstructure characterization

The microstructures of samples were characterized by X-ray diffraction (XRD, Philips X'pert MPD) with Cu-K_α radiation, field-emission scanning electron microscopy (FE-SEM, Carl Zeiss Supra 40), and transmission electron microscopy (TEM, JEOL-2100) at 200 kV. The electronic states of Sn in the composite were determined by X-ray photoelectron spectrometry (XPS, AXIS Ultra DLD) using Al-K_α radiation. The tap density of the powders was tested according to the Chinese standard GB/T 5162-2006/ISO 3953:1993. The contents of Sn, C and O were measured by electron probe X-ray microanalysis (EPMA, EPMA-1600). The degree of graphitization of the carbon after milling was measured by a LabRam Aramis

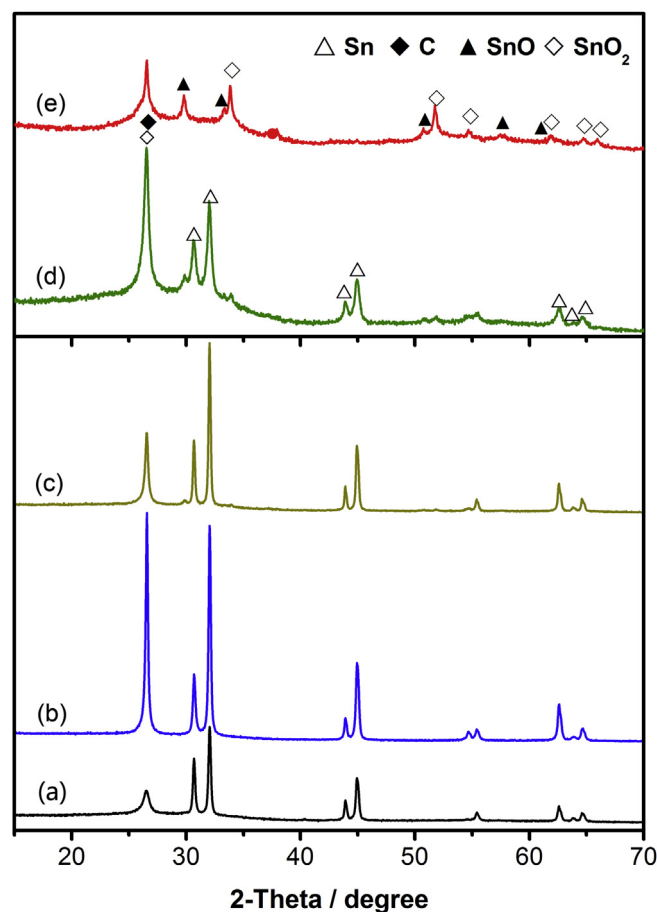


Fig. 2. XRD patterns of (a) Sn–C composite obtained by P-milling, and Sn@SnO_x/C composites prepared by O₂-P-milling: (b) Sn@SnO_x/C-2 h, (c) Sn@SnO_x/C-5 h, (d) Sn@SnO_x/C-10 h, and (e) SnO_x/C.

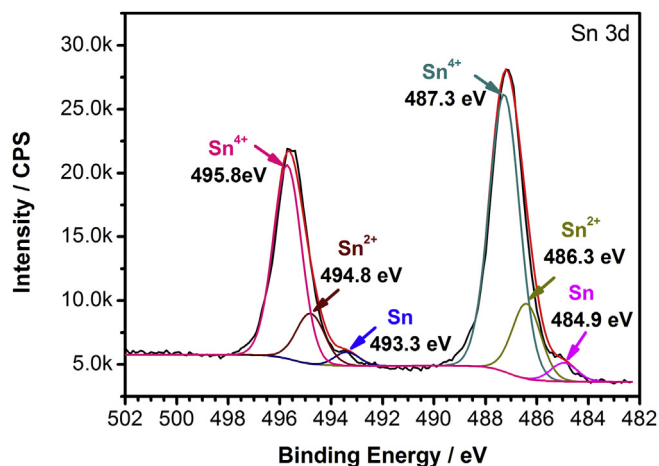


Fig. 3. Sn 3d core level XPS for the Sn@SnO_x/C-10 h composite.

spectrometer at a 632.8 nm excitation wavelength. Cycled electrodes were washed several times with diethyl carbonate (DEC) and absolute ethanol to remove the electrolyte before microstructure analysis.

2.3. Electrochemical measurements

The electrochemical properties of the as-prepared composites were measured using coin-type half-cells (CR2016) assembled in an argon-filled glove box with lithium ribbon serving as the counter and reference electrodes. The working electrode consisted of 80 wt % active powder, 10 wt% Super-P, and 10 wt% PVDF. The loading of active materials was 1–1.5 mg cm⁻². The electrolyte was LiPF₆ (1 M) in a mixture of ethylene carbonate (EC)/DEC/ethyl methyl carbonate (EMC) (1:1:1, v:v:v) (Shanshan Tech Co., Ltd.). Galvanostatic charge–discharge measurements were performed with battery testers (BT-2000, Arbin Instruments, USA) at various current densities in the range of 0.01–1.5 V vs. Li/Li⁺. CV was performed with an electrochemical system (AutoLab) over the potential range 0.0–2.0 V vs. Li/Li⁺ at scan rates of 0.3, 0.5, 0.7, 0.9, and 1.2 mV s⁻¹. All the electrochemical tests were carried out at ambient temperature.

3. Results and discussion

3.1. Microstructure of Sn@SnO_x/C composites

Fig. 2 shows XRD patterns of Sn–C composite prepared by P-milling, Sn@SnO_x/C and SnO_x/C composites prepared by O₂-P-milling for different periods. The peak located at 26.6° was attributed to the diffraction of graphite, and peaks at 30.6 and 32.0° were indexed as Sn in Fig. 2(a). Peaks consistent with tetragonal Sn weakened and widened significantly as the O₂-P-milling time increased, suggesting a distinct refinement of Sn grain size and a gradual decrease in the amount of Sn. Eventually, for the SnO_x/C composite shown in Fig. 2(e), the diffraction peaks of Sn became undistinguishable. The average grain size of Sn in the Sn@SnO_x/C-10 h composite was calculated to be 27 nm using the Voigt function, which was much smaller than that in the Sn–C composite (68 nm). In the pattern of the Sn@SnO_x/C-5 h composite (Fig. 2(c)), weak characteristic diffraction peaks of SnO (2θ of 29.8 and 33.3°) and SnO₂ (2θ of 33.9°) emerged. In the diffraction patterns of the Sn@SnO_x/C-10 h and SnO_x/C composites, these peaks got stronger (Fig. 2(d) and (e)), and two broad humps located at around 28° and

55° were detected, which could be attributed to amorphous SnO_x [34,35]. Overall, the XRD results revealed that there were amorphous and nanocrystalline SnO_x ($1 \leq x \leq 2$) phases coexisting in the Sn@SnO_x/C-10 h and SnO_x/C composites.

Fig. 3 shows the XPS results of the Sn@SnO_x/C-10 h composite. The dominant signals at 487.3 and 495.8 eV were assigned to Sn⁴⁺, while the two peaks at 486.3 and 494.8 eV were ascribed to Sn²⁺ while the weakest peaks at 484.9 and 493.3 eV corresponded to Sn⁰. This further confirmed that the existence of SnO_x formed on the surface of the composite after O₂-P-milling for 10 h. EPMA showed the content of O in the Sn@SnO_x/C-10 h composite were 7.7 wt%, from which the content of SnO_x could be calculated ranging from 36.5 wt% (SnO) to 65.2 wt% (SnO₂). Considering that 46.4 wt% C was detected in the composite, the content of SnO_x was further estimated to be in the range of 36.5–53.6 wt%. Similarly, the content of SnO_x could be estimated 53.6–63.7 wt% in the SnO_x/C composite based on the EPMA results (11.4 wt% O and 36.3 wt% C). Additionally, the content of carbon in the SnO_x/C was lower than that in Sn@SnO_x/C-10 h, indicating more graphite was lost during O₂-P-milling, which might be converted into CO and/or CO₂ etc.

To evaluate the impact of O₂-P-milling on graphite, a comparison of Raman spectra for Sn@SnO_x/C-10 h and Sn–C composites was carried out as shown in Fig. 4. The peaks located at 1322 and 1565 cm⁻¹ correspond to the characteristic D and G bands of carbon, respectively. The I_D/I_G ratio was 0.491 in Sn@SnO_x/C-10 h composite, which was nearly equal to that of Sn–C composite (0.489), suggesting the crystallinity of graphite was not dramatically decreased under O₂-P-milling compared with P-milling. Based on the above results, we could conclude that SnO_x was formed, while Sn and crystalline graphite were remained as the dominant phases in the O₂-P-milled Sn@SnO_x/C-10 h composite as expected, and the composite exhibited a high tap density of 1.33 g cm⁻³.

Backscattered electron SEM images of the Sn@SnO_x/C-2 h, -5 h, -10 h, and Sn–SnO₂-C for comparison are presented in Fig. 5. When the O₂-P-milling time was 2 h (Fig. 5(a)), the Sn-rich phases (bright zones) were large floccules dispersed in the graphite matrix (dark zones). With increasing milling time, the dispersion of Sn in the graphite matrix became more even. This differed considerably from the morphology of the Sn–SnO₂-C composite obtained by P-milling for 10 h, where the Sn particles, as indicated by arrows in Fig. 5(d), were clearly visible and larger than those in the O₂-P-milled composites. It suggested that the SnO_x formed *in situ* on the Sn surface during O₂-P-milling was more beneficial for the

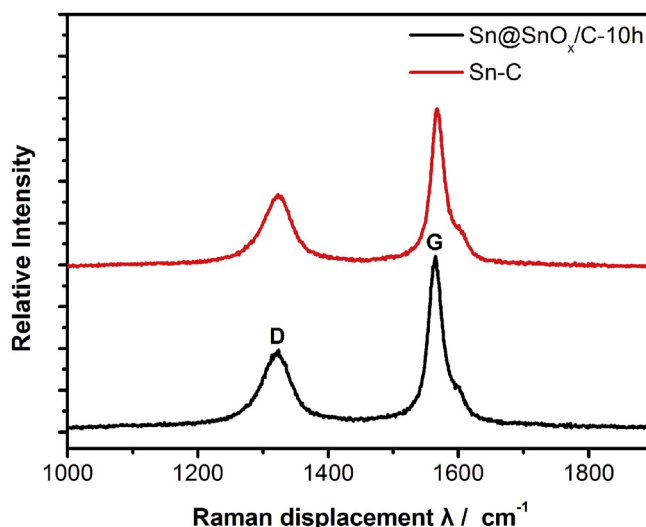


Fig. 4. Raman spectra of Sn–C and Sn@SnO_x/C-10 h composites.

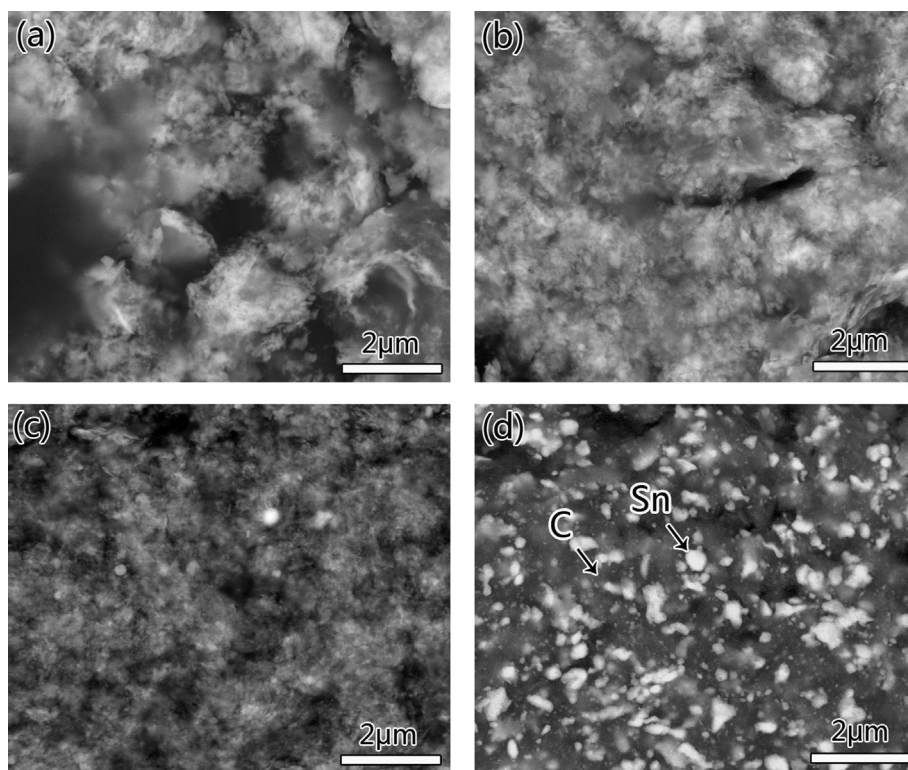


Fig. 5. Backscattered electron SEM images of (a) Sn@SnO_x/C-2 h, (b) Sn@SnO_x/C-5 h, (c) Sn@SnO_x/C-10 h, and (d) Sn-SnO₂-C composites.

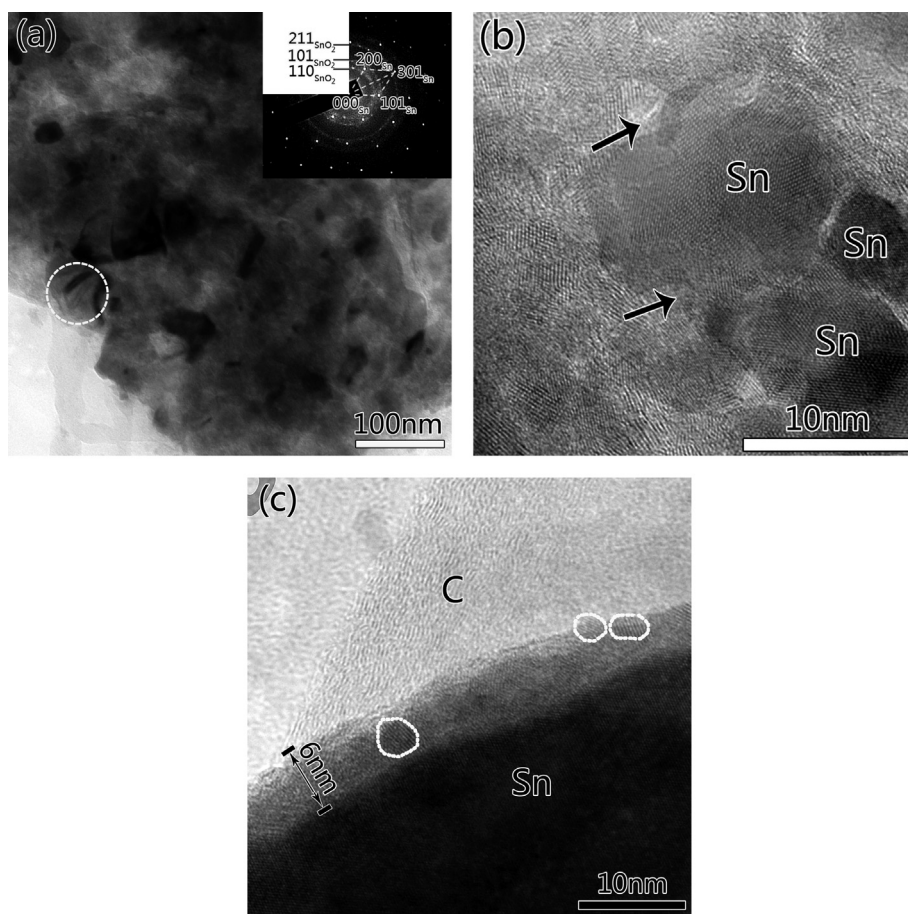


Fig. 6. (a) Bright-field TEM image and SAED pattern (inset at top-right) of the Sn@SnO_x/C-10 h composite. (b) and (c) HRTEM images of typical microstructures in the Sn@SnO_x/C-10 h composite.

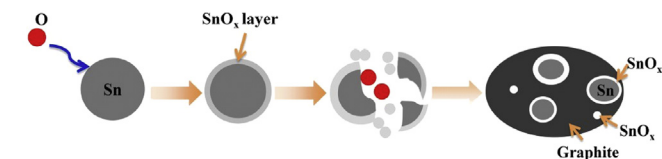


Fig. 7. Schematic diagram of the formation mechanism for the Sn@SnO_x/C composite by O₂-P-milling.

refinement and dispersion of Sn than the SnO₂ additive. As a result, it was expected that the Sn@SnO_x/C-10 h composite would exhibit better electrochemical performance than the Sn–SnO₂–C composite.

To further investigate the morphology and distribution of Sn and SnO_x in the graphite matrix, the Sn@SnO_x/C-10 h composite was characterized by TEM. As shown in Fig. 6(a), nanosized Sn and SnO_x particles were embedded in the graphite matrix. The circled particle in Fig. 6(a) consisted of a single-crystalline Sn phase and nanocrystalline SnO₂, as revealed by their selected-area electron diffraction (SAED) patterns (inset of Fig. 6(a)). There were two typical distributions of SnO_x in the Sn@SnO_x/C-10 h composite: (1) amorphous SnO_x separated from Sn by milling (indicated by arrows in Fig. 6(b)), and (2) a 6–10 nm-thick amorphous/nanocrystalline SnO_x layer coated on a single-crystalline Sn embedded in graphite matrix (Fig. 6(c)). The latter core–shell structure was generally dominant in the Sn@SnO_x/C-10 h composites prepared by O₂-P-milling, and was exactly the structure we anticipated.

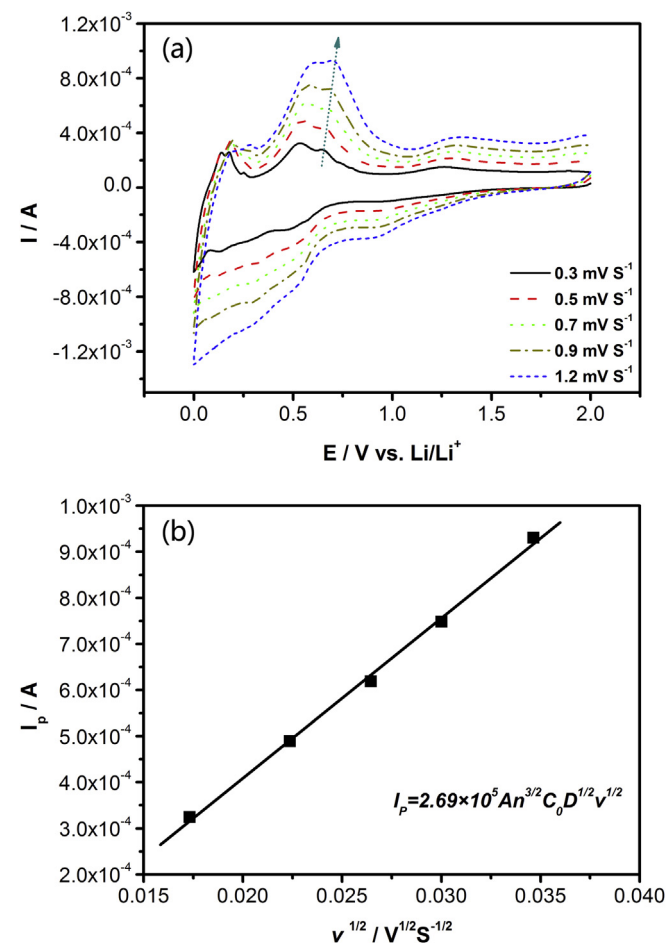


Fig. 8. (a) Cyclic voltammograms in the potential range 0.0–2.0 V at scanning rates of 0.3, 0.5, 0.7, 0.9, and 1.2 mV s^{−1}, and (b) the relationship between I_p and $v^{1/2}$ for the Sn@SnO_x/C-10 h composite.

A deduced forming mechanism of Sn@SnO_x/C composite was presented schematically in Fig. 7. First, SnO_x nucleated on the surface of Sn particles in the oxygen-plasma field, resulting in a core–shell structure as SnO_x grew. SnO_x partly exfoliated as the strain accumulated, exposing fresh surface of Sn. With the grinding aid of rigid SnO_x nanoparticles, Sn was gradually refined due to the synergistic effects of heating and stress. Meanwhile, new SnO_x would then form on the surface of the refined Sn. It is important to note that a stable SnO_x layer (only about 1–2 nm) is able to form on the Sn particles in the air. However, the SnO_x layer would grow according to the Mott–Cabrera theory [36,37], because of the charge field and rapid heating during O₂-P-milling. Accordingly, a 6–10 nm-thick SnO_x layer could be observed, as shown in Fig. 6(c). Moreover, the content of SnO_x in the composite could be enhanced by increasing the oxygen input and milling time. It was expected that the graphite matrix, as well as the Li₂O formed by the reaction of SnO_x with Li⁺ in the first discharge, could effectively buffer the volume expansion of Sn and prevent the aggregation of the nano-sized active materials during cycling, thereby maintaining the stability of the electrode.

3.2. Electrochemical performance of Sn@SnO_x/C composite anodes

To investigate the kinetics of lithium intercalation/deintercalation into/from the Sn@SnO_x/C-10 h electrode, a series of CV

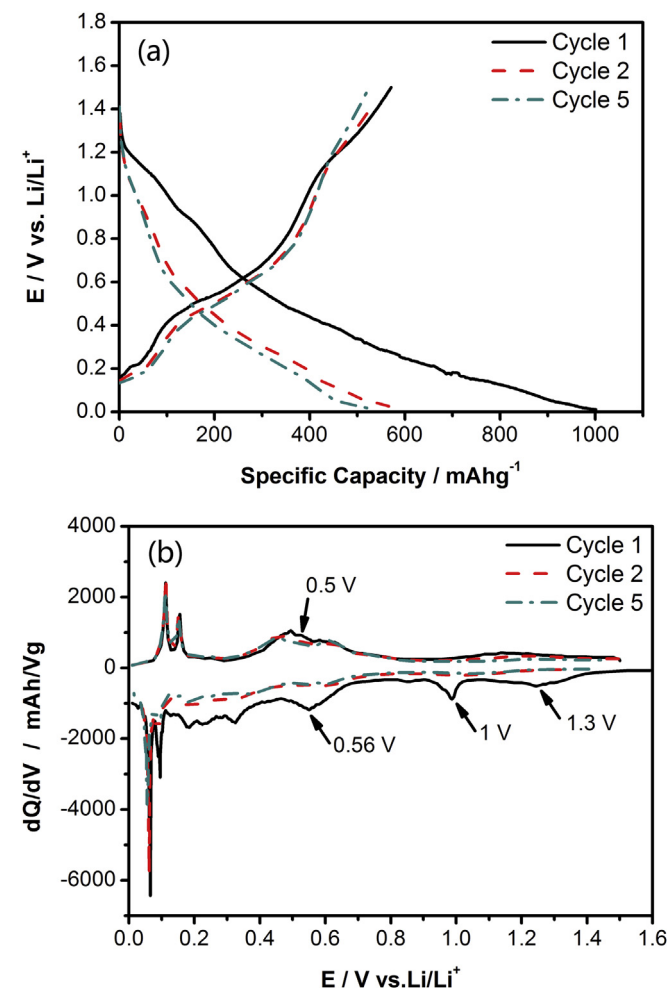


Fig. 9. (a) Initial discharge–charge profiles, and (b) differential capacity vs. potential plots for the Sn@SnO_x/C-10 h composite. Current density: 0.4 mA cm^{−2} (about 250 mA g^{−1}), cut-off potential: 0.01–1.5 V.

curves were recorded. As shown in Fig. 8(a), an increase in scan rate v caused a progressive shift of the anodic peaks to higher potential as well as an increase in peak height. The linear relationship between I_p and $v^{1/2}$ (Fig. 8(b)) indicates that the reaction kinetics were controlled by the diffusion of Li, as suggested by the Randles–Sevcik equation (Eq. (3)) [38–40]:

$$I_p = 2.69 \times 10^5 n^{3/2} A D^{1/2} v^{1/2} C_0 \quad (3)$$

where A is the electrode area (0.5 cm^2 in this work), n is the number of electrons involved in the reaction (Li^+ , $n = 1$), C_0 is the concentration of Li^+ in the solution (mol cm^{-3}), and D is the diffusion coefficient of Li^+ (D_{Li^+} , $\text{cm}^2 \text{ s}^{-1}$). Based on Eq. (3), D_{Li^+} for the $\text{Sn@SnO}_x/\text{C}$ -10 h composite was estimated to be $6.68 \times 10^{-7} \text{ cm}^2 \text{ s}^{-1}$, which is one order of magnitude higher than that of the P-milled Sn-C composite ($2.7 \times 10^{-8} \text{ cm}^2 \text{ s}^{-1}$) and three orders of magnitude higher than that of pure SnO_2 ($7.2 \times 10^{-10} \text{ cm}^2 \text{ s}^{-1}$) [41]. The high Li^+ diffusion coefficient in the $\text{Sn@SnO}_x/\text{C}$ -10 h composite is attributed to the unique nanostructure of this material. A short Li^+ diffusion distance was provided by the refined Sn nanoparticles after O_2 -P-milling and the nanocrystalline Li_2O and Sn formed along high-density grain boundaries of amorphous/nanocrystalline SnO_x would promote the diffusion/drift of Li ions [42]. Moreover, the graphite matrix could maintain the conductive network for the active phases. All of these features implied that the $\text{Sn@SnO}_x/\text{C}$ -10 h composite should exhibit good lithium storage performance.

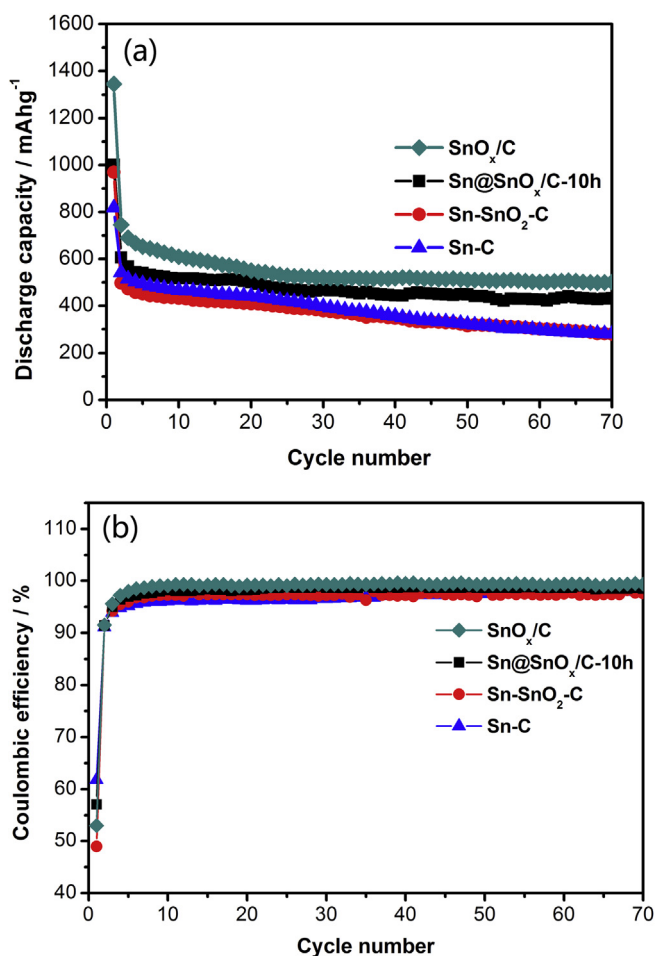


Fig. 10. Comparison of cycle performance for the $\text{Sn@SnO}_x/\text{C}$ -10 h, SnO_x/C , $\text{Sn-SnO}_2\text{-C}$, and Sn-C composites between 0.01 and 1.5 V at 250 mA g^{-1} : (a) discharge capacity vs. cycle number, and (b) coulombic efficiency vs. cycle number.

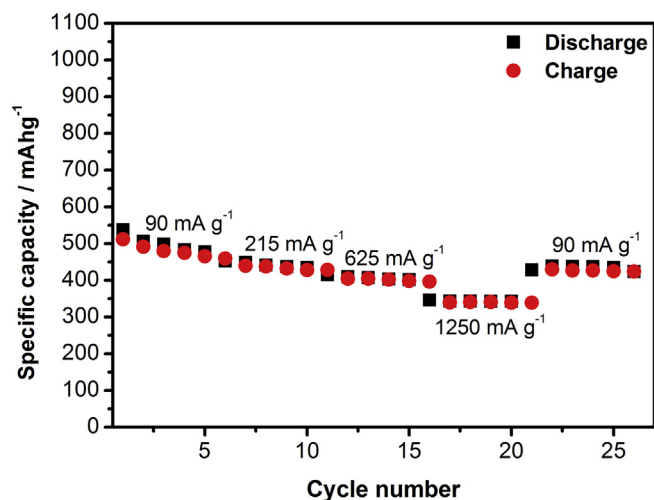


Fig. 11. Rate capability of the $\text{Sn@SnO}_x/\text{C}$ -10 h composite. Cut-off potential: 0.01–1.5 V.

Fig. 9(a) shows the 1st, 2nd and 5th discharge–charge profiles of the $\text{Sn@SnO}_x/\text{C}$ -10 h composite at a constant current density of 0.4 mA cm^{-2} (about 250 mA g^{-1}). The first discharge and charge capacities were 1001.1 and $571.2 \text{ mA h g}^{-1}$, respectively, implying an initial coulombic efficiency of 57.1%. The irreversible capacity loss was mainly attributed to the formation of Li_2O in the irreversible reduction of SnO_x to Sn and SEI film formation at 1.2–0.8 V [20,43]. The initial coulombic efficiency was slightly lower than that of the Sn-C composite (61.8%), but substantially higher than those for previously reported SnO_2 materials [19,44,45]. The differentials of the capacity vs. potential curves are presented in Fig. 9(b). Two peaks at potentials of around 1.3 and 1.0 V were observed in the first scan but disappeared in subsequent cycles, which indicated the irreversible reaction between Li and SnO_x (Eq. (1)). In addition, two pairs of redox peaks at 0.075/0.1 and 0.1/0.15 V were related to the intercalation/extraction of lithium into/from graphite during the discharge/charge process. Only broad peaks corresponding to lithium alloying/dealloying with the pure Sn phase were observed between 0.4 and 0.8 V in the first scan, which was presumably related to the small grain size of the Sn. These results suggested that graphite, nanosized Sn together with SnO_x

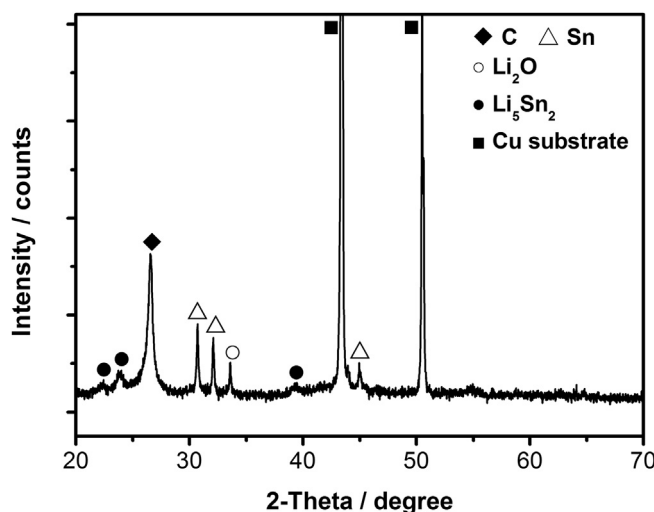


Fig. 12. XRD pattern of the $\text{Sn@SnO}_x/\text{C}$ -10 h composite after three discharge-charge cycles.

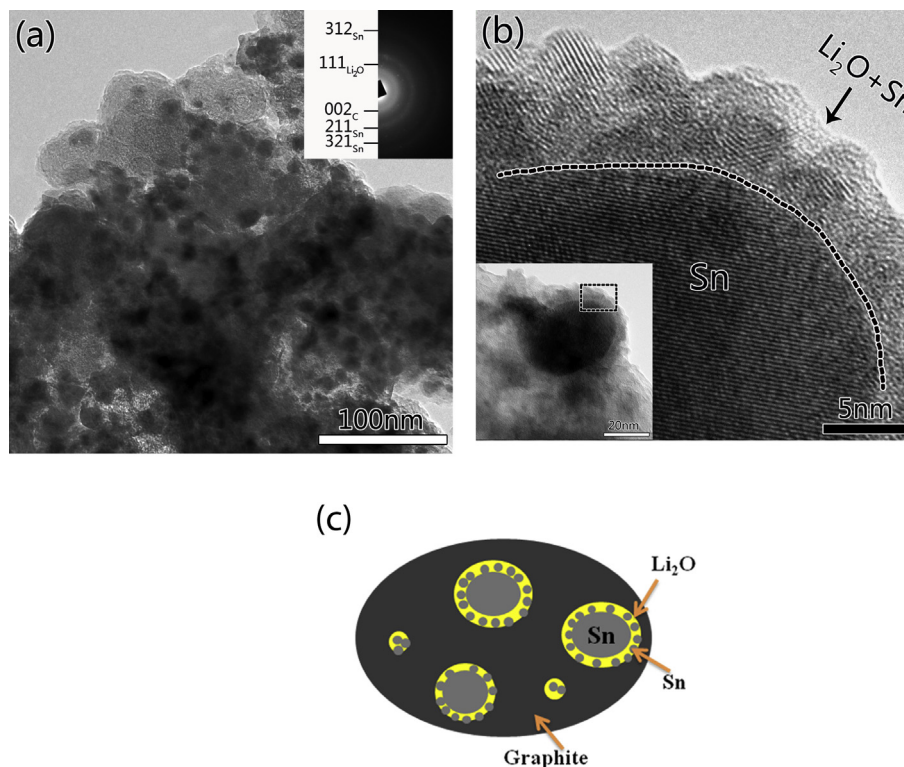


Fig. 13. (a) Bright-field TEM image with a SAED pattern (inset at top-right) of the Sn@SnO_x/C-10 h composite after three discharge–charge cycles. (b) HRTEM image of the area highlighted by a dotted rectangle. (c) Schematic diagram of microstructure evolution for the Sn@SnO_x/C-10 h composite after Li alloying and dealloying.

contributed to the total capacity of the electrode. Taking fully into account the capacity contribution from P-milled graphite (160 mA h g^{-1}) [29], Sn, and SnO_x in which its reversible capacity just depended on the capacity released by the Sn contained, the theoretical reversible capacities of the Sn@SnO_x/C-10 h was evaluated to be about 530 mA h g^{-1} ($992 \times 45.9\% + 160 \times 46.4\% = 530 \text{ mA h g}^{-1}$). Similarly, the theoretical reversible capacity of SnO_x/C was calculated to be 580 mA h g^{-1} .

Fig. 10 depicts the cycle performance of the SnO_x/C, Sn@SnO_x/C, Sn–SnO₂–C, and Sn–C composite electrodes at a constant current density of 250 mA g^{-1} . Sn@SnO_x/C-10 h showed a capacity of about 430 mA h g^{-1} after 70 cycles, and a high coulombic efficiency of 98.9% after the initial five cycles, while Sn–SnO₂–C and Sn–C exhibited less than 300 mA h g^{-1} after 70 cycles. It demonstrated that the capacity and cyclic stability of Sn@SnO_x/C-10 h were much improved compared with those of Sn–SnO₂–C, and Sn–C. By increasing the oxygen content and milling time, the cycle performance of the Sn@SnO_x/C composite could be further enhanced: SnO_x/C maintained a capacity of 500 mA h g^{-1} for 70 cycles with a higher coulombic efficiency of 99.4%, although its first irreversible capacity (632 mA h g^{-1}) was higher than that of Sn@SnO_x/C-10 h (429 mA h g^{-1}). The improved capacity retention in SnO_x/C should be attributed to the higher content of amorphous/nanocrystalline SnO_x compared with that in Sn@SnO_x/C-10 h. Firstly, as the milled time expanding from 10 h to 25 h, the active Sn generated from SnO_x would be smaller and dispersed inside the matrix more evenly than that in Sn@SnO_x/C-10 h. The finer Sn was more beneficial to discharge/charge in depth to release capacity and more tolerant for the volume change in the following cycles. Second, more Li₂O, resulted from the reaction of SnO_x with lithium, could buffer the volume change and prevent the aggregation of the active materials, which relieved the structure damage of the composite. The latter was also a main reason why SnO_x/C showed a lower initial coulombic efficiency of 53% than 57.1% in Sn@SnO_x/C-10 h

(Fig. 10(b)). Nevertheless, the first coulombic efficiency of SnO_x/C was still 4% higher than that for the Sn–SnO₂–C composite with 5 wt% SnO₂ (49.0%).

Fig. 11 shows the rate capability of the Sn@SnO_x/C-10 h electrode after three activation cycles. The Sn@SnO_x/C-10 h composite maintained a stable reversible capacity of 340 mA h g^{-1} at a high current density of 1250 mA g^{-1} . A capacity of 430 mA h g^{-1} could be restored when the current density was reduced to 90 mA g^{-1} . The superior rate capability was attributed to the enhanced kinetics resulted from the short diffusion distance for Li⁺ intercalation in the nanoparticles of Sn@SnO_x/C-10 h.

To further investigate the advantageous features of the Sn@SnO_x/C composites, the microstructure evolution of Sn@SnO_x/C-10 h composite electrode after three cycles was analyzed by XRD and TEM. The XRD pattern in Fig. 12 indicated that graphite and Sn were the dominant phases in addition to the substrate Cu. Diffraction peaks attributed to Li₂O and Li₅Sn₂ were observed, while no diffraction peaks consistent with SnO_x could be detected, which demonstrated the lithium storage mechanism of SnO_x (Eq. 1 and 2). A bright-field TEM image (Fig. 13(a)) indicated that the Sn nanoparticles were still homogeneously embedded in the graphite matrix after three cycles, without obvious aggregation. In the SAED pattern (the inset of Fig. 13(a)), diffraction rings of Sn (211), (321), (312), C (002), and Li₂O (111) confirmed their nanocrystalline nature. HRTEM images (Fig. 13(b)) revealed the well-maintained core–shell structure, and the Sn nanoparticles surrounded by a layer of amorphous/nanocrystalline Li₂O and Sn could be clearly observed. Therefore, the microstructure evolution of the Sn@SnO_x/C-10 h composite after Li alloying and dealloying (illustrated in Fig. 13(c)) could reveal the reasons for its superior cyclability: (1) Sn and SnO_x nanoparticles refined by O₂–P-milling could withstand large volume changes during Li alloy/dealloy. (2) Graphite and Li₂O generated from SnO_x during the first discharge accommodated the volume expansion of Sn, effectively preventing aggregation of the

Sn nanoparticles. Both of these factors inhibited the pulverization of the electrode, due to which the continual breakdown and reformation of the SEI was suppressed, and the electric contact between the electrode and matrix was maintained. In short, the unique microstructure of the O₂-P-milled Sn@SnO_x/C composite maintained the stability of the electrode during cycling and led to excellent cycle performance.

4. Conclusion

In summary, a facile and highly efficient one-step strategy, O₂-P-milling, has been developed for the synthesis of Sn@SnO_x/C composites as lithium ion anode materials. The composites had a unique microstructure of amorphous/nanocrystalline Sn@SnO_x embedded in a graphite matrix. The Sn nanoparticles could undergo volume change during Li intercalation and extraction, and the graphite and Li₂O could prevent aggregation of the Sn nanoparticles, which resulted in excellent cyclability with a high stable capacity of 430 and 500 mA h g⁻¹ at 250 mA g⁻¹ in the Sn@SnO_x/C-10 h and SnO_x/C composite, respectively. The O₂-P-milling could be extended to other material systems such as Si@SiO_x/C composites, which is promising in the large-scale production of anode materials with high capacity retention.

Acknowledgements

This work was supported by the National Science Foundation of China under project nos. 51201065, and 51231003, Guangdong National Science Foundation under project no. S2012040008050, the Fundamental Research Funds for the Central Universities under project no. 2012ZM0001 and KLGHEI (KLB11003).

References

- [1] A.D.W. Todd, P.P. Ferguson, M.D. Fleischauer, J.R. Dahn, *Int. J. Energy Res.* 34 (2010) 535–555.
- [2] N.C. Li, C.R. Martin, *J. Electrochem. Soc.* 148 (2001) A164–A170.
- [3] I.A. Courtney, J.R. Dahn, *J. Electrochem. Soc.* 144 (1997) 2045–2052.
- [4] A. Sivashanmugam, T.P. Kumar, N.G. Renganathan, S. Gopukumar, M. Wohlfahrt-Mehrens, J. Garche, *J. Power Sources* 144 (2005) 197–203.
- [5] Y. Kim, Y. Yoon, D. Shin, *J. Anal. Appl. Pyrol.* 85 (2009) 557–560.
- [6] P. Meduri, C. Pendyala, V. Kumar, G.U. Sumanasekera, M.K. Sunkara, *Nano Lett.* 9 (2009) 612–616.
- [7] G. Derrien, J. Hassoun, S. Panero, B. Scrosati, *Adv. Mater.* 19 (2007) 2336–2340.
- [8] A.D.W. Todd, R.E. Mar, J.R. Dahn, *J. Electrochem. Soc.* 154 (2007) A597–A604.
- [9] J.Z. Chen, L. Yang, S.H. Fang, S.-i Hirano, *Electrochem. Commun.* 13 (2011) 848–851.
- [10] Y.G. Wang, B. Li, C.L. Zhang, H. Tao, S.F. Kang, S. Jiang, X. Li, *J. Power Sources* 219 (2012) 89–93.
- [11] R.B. Lewis, A. Timmons, R.E. Mar, J.R. Dahn, *J. Electrochem. Soc.* 154 (2007) A213–A216.
- [12] Y. Tian, A. Timmons, J.R. Dahn, *J. Electrochem. Soc.* 156 (2009) A187–A191.
- [13] L.Y. Beaulieu, K.W. Eberman, R.L. Turner, L.J. Krause, J.R. Dahn, *Electrochem. Solid-State Lett.* 4 (2001) A137–A140.
- [14] P.P. Ferguson, M. Rajora, R.A. Dunlap, J.R. Dahn, *J. Electrochem. Soc.* 156 (2009) A204–A208.
- [15] L.Y. Beaulieu, J.R. Dahn, *J. Electrochem. Soc.* 147 (2000) 3237–3241.
- [16] P.P. Ferguson, P. Liao, R.A. Dunlap, J.R. Dahn, *J. Electrochem. Soc.* 156 (2009) A13–A17.
- [17] F. Han, W.C. Li, M.R. Li, A.H. Lu, *J. Mater. Chem.* 22 (2012) 9645–9651.
- [18] X.W. Lou, C.M. Li, L.A. Archer, *Adv. Mater.* 21 (2009) 2536–2539.
- [19] S.J. Ding, J.S. Chen, X.W. Lou, *Chem.-Asian J.* 6 (2011) 2278–2281.
- [20] P. Wu, N. Du, H. Zhang, C.X. Zhai, D. Yang, *ACS Appl. Mater. Interfaces* 3 (2011) 1946–1952.
- [21] Y.H. Xu, J.C. Guo, C.S. Wang, *J. Mater. Chem.* 22 (2012) 9562–9567.
- [22] Y. Wang, H.C. Zeng, J.Y. Lee, *Adv. Mater.* 18 (2006) 645–649.
- [23] W.M. Zhang, J.S. Hu, Y.G. Guo, S.F. Zheng, L.S. Zhong, W.G. Song, L.J. Wan, *Adv. Mater.* 20 (2008) 1160–1165.
- [24] R.Q. Liu, N. Li, D.Y. Li, G.F. Xia, Y.M. Zhu, S.Y. Yu, C. Wang, *Mater. Lett.* 73 (2012) 1–3.
- [25] Y.S. Lin, J.G. Duh, M.H. Hung, *J. Phys. Chem. C* 114 (2010) 13136–13141.
- [26] L. Zou, L. Gan, R. Lv, M.X. Wang, Z.H. Huang, F.Y. Kang, W.C. Shen, *Carbon* 49 (2011) 89–95.
- [27] H.R. Jung, W.J. Lee, *J. Electroanal. Chem.* 662 (2011) 334–342.
- [28] Y. Yu, L. Gu, C.L. Wang, A. Dhanabalan, P.A. van Aken, J. Maier, *Angew. Chem. Int. Ed.* 48 (2009) 6485–6489.
- [29] H. Liu, R.Z. Hu, M.Q. Zeng, J.W. Liu, M. Zhu, *J. Mater. Chem.* 22 (2012) 8022–8028.
- [30] Y.S. Hu, R. Demir-Cakan, M.M. Titirici, J.O. Müller, R. Schlögl, M. Antonietti, J. Maier, *Angew. Chem. Int. Ed.* 47 (2008) 1645–1649.
- [31] H. Wu, G. Chan, J.W. Choi, I. Ryu, Y. Yao, M.T. McDowell, S.W. Lee, A. Jackson, Y. Yang, L. Hu, Y. Cui, *Nat. Nano* 7 (2012) 310–315.
- [32] L.Y. Dai, B. Cao, M. Zhu, *Acta Metall. Sin. (Engl. Lett.)* 19 (2006) 411–417.
- [33] M. Zhu, L.Y. Dai, N.S. Gu, B. Cao, L.Z. Ouyang, *J. Alloys Compd.* 478 (2009) 624–629.
- [34] M. Zadsar, H.R. Fallah, M. Haji Mahmoodzadeh, A. Hassanzadeh, M. Ghasemi Varnamkhasti, *Mater. Sci. Semicon. Proc.* 15 (2012) 432–437.
- [35] G.F. Ortiz, P. Lavela, P. Knauth, T. Djenizian, R. Alcántara, J.L. Tirado, *J. Electrochem. Soc.* 158 (2011) A1094–A1099.
- [36] S. Sako, K. Ohshima, T. Fujita, *J. Phys. Soc. Jpn.* 59 (1990) 662–666.
- [37] N. Cabrera, N.F. Mott, *Rep. Prog. Phys.* 12 (1949) 163–184.
- [38] J.R. Dahn, J.W. Jiang, L.M. Moshurhak, M.D. Fleischauer, C. Buhrmester, L.J. Krause, *J. Electrochemical Soc.* 152 (2005) A1283–A1289.
- [39] R.Z. Hu, H. Liu, M.Q. Zeng, J.W. Liu, M. Zhu, *J. Mater. Chem.* 22 (2012) 9539–9545.
- [40] M. Mancini, P. Kubiak, M. Wohlfahrt-Mehrens, R. Marassi, *J. Electrochem. Soc.* 157 (2010) A164–A170.
- [41] L.F. Cui, J. Shen, F.Y. Cheng, Z.L. Tao, J. Chen, *J. Power Sources* 196 (2011) 2195–2201.
- [42] S.C. Kweon, I.H. Oh, J.K. Lee, A.A. Khodin, *Mater. Lett.* 83 (2012) 88–90.
- [43] S.J. Ding, J.S. Chen, G.G. Qi, X.N. Duan, Z.Y. Wang, E.P. Giannelis, L.A. Archer, X.W. Lou, *J. Am. Chem. Soc.* 133 (2010) 21–23.
- [44] L.M. Li, X.M. Yin, S. Liu, Y.G. Wang, L.B. Chen, T.H. Wang, *Electrochem. Commun.* 12 (2010) 1383–1386.
- [45] C.H. Yim, E.A. Baranova, F.M. Courtel, Y. Abu-Lebdeh, I.J. Davidson, *J. Power Sources* 196 (2011) 9731–9736.